Journal of The Electrochemical Society, **150** (6) A783-A789 (2003) A783
0013-4651/2003/150(6)/A783/7/$7.00 © The Electrochemical Society, Inc.

Modeling of Mass and Heat Transport in Planar Substrate Type SOFCs

T. Ackmann, L. G. J. de Haart,*,z W. Lehnert,*,a and D. Stolten

Forschungszentrum Jülich GmbH, Institute for Materials and Processes in Energy Systems, Energy Process Engineering, D-52425 Jülich, Germany

A mathematical model is presented that incorporates the mass transport by diffusion in the porous structure of thick substrate type solid oxide fuel cells (SOFCs). On the basis of the mean transport pore model a multidimensional study allows for an optimization of the structural parameters of the substrates with respect to cell performance. Next to the mass transport in the porous substrates the electrochemical kinetics, methane/steam reforming and shift reaction, and energy equations are integrated in the model and boundary as well as operation conditions can be varied. Two-dimensional simulations for both anode as well as cathode substrate type SOFC operating on partially prereformed methane are presented and discussed.
 [DOI: 10.1149/1.1574029]

Manuscript submitted February 25, 2002; revised manuscript received July 18, 2002. Available electronically April 28, 2003.

Mathematical modeling of solid oxide fuel cells (SOFCs) is a helpful tool in examining various design and operation parameters such as geometry, dimensions, fuels, temperatures, and pressures. With the appropriate models and parameter values influences on gas concentration, temperature, current density, and stress distributions can be determined. Results can be used to optimize designs and select optimal operation conditions. During recent years, a number of mathematical models have been published on mass and heat transport in SOFC stacks.[1-5] Most models considered the direction of fuel gas flow only, to determine the concentration and temperature profiles in either a tubular or planar type SOFC. The actual cell (anode/electrolyte/cathode) is treated as one solid component with averaged properties. Until recently, such an approximation was sufficient for the standard planar concept with a relatively thick supporting electrolyte, because only the main balances of a cell or stack were analyzed. However, more recently, the planar concept with a thin electrolyte layer supported on a thick substrate formed by one of the electrodes has gained much more interest.[6-9] This development of the so-called substrate concept is aimed at a reduction of the operation temperature of the SOFC to below 800°C. Thus, the anode/electrolyte/cathode assembly can no longer be treated as one solid component. Mass transport in the thick substrate, which can be either the anode or the cathode, must be considered. The diffusion path length for the gases from the gas channel to the three-phase boundary (TPB) can be as long as 1.5 mm which as a consequence can result in diffusion limitations. Furthermore, an anode substrate leads to a spatial separation of the reforming reaction and the electrochemical reactions, the latter being restricted to only a very thin (<20 μm) region at the electrode/electrolyte interface.

Yakabe *et al.*[10,11] performed three-dimensional simulations for a complete anode substrate cell using the parallel pore model to describe mass transport by diffusion in the thick porous anode. In our group a one-dimensional isothermal model was developed previously, based on the mean transport pore model[12] (MTPM) to describe mass transport of gases in porous electrodes, and including the reforming reaction and the electrochemistry for an anode substrate concept.[13] Energy balances were implemented to consider nonisothermal behavior.[14] The major difference between our calculations and the aforementioned simulations of Yakabe *et al.* is the model used to describe the mass transport in the porous electrodes. The MTPM has an advantage over the parallel pore model, that both the permeability coefficient and the diffusion coefficient are calculated from structural parameters of the porous material, which can be determined directly for real components by permeation and diffusion experiments in a Wicke-Kallenbach cell. In this paper we describe the extension of the existing model to two dimensions. The analysis emphasizes mass transport in porous electrodes, especially in the problematical zone below the interconnect ribs. Furthermore, the cathode substrate concept is considered as well, which has not been done before.

Model

The model was developed for a SOFC based on a planar substrate type concept. The fuel cell is considered to operate on either hydrogen or a (prereformed) methane/steam mixture as fuel and oxygen from air as oxidant. Next to the description of the electrochemical reactions, the methane/steam reforming and shift reactions, the heat-transfer and the mass-transfer processes are included in the model. Distinct from previous models, the fuel and oxidant flow, *i.e.*, multicomponent transport, were developed for a realistic fuel cell comprising porous elements, based on a finite-volume-based computational fluid dynamics (CFD) approach. For this purpose the model calculations were performed using the commercial CFD-package FLUENT.

Model assumptions.—Ideal gas mixtures, incompressible and laminar flow due to small gas velocities, and pressure gradients are assumed. The electrodes have a homogeneous, isotropic structure and no gradients within mechanical properties. The electrolyte is regarded as an infinite thin layer between anode and cathode. In the model the mass and heat sources according to the electrochemical conversion arise in the boundary cells of the anode next to the electrolyte. The thickness of these boundary cells depends on the truncation grade of the anode.

Fuel cell geometry.—Figure 1 is a schematic diagram for a planar SOFC concept using either a cathode or an anode substrate. Air diffuses from the air channels into the cathode and reacts electrochemically at the TPB. Gas channels are realized in the interconnect. The width of the gas channels and the interconnect ribs for current passage are equivalent. The dimensions of the components used in the calculations are given in Table I. In the calculations only half of both the channel and the interconnect are considered because of the symmetry perpendicular to the direction of the gas flow. The balance room as indicated in Fig. 1 thus consists of the porous electrodes under the channels and interconnects. Boundary conditions are set accordingly at the interfaces of the electrodes with the gas channels and the interconnect ribs.

In contrast to the cathode substrate, the anode substrate shown in Fig. 1a consists of a thick supporting anode and a thin cathode. The fuel gas that flows through the fuel gas channel, diffuses into the porous anode and, in hydrocarbon fuel, is reformed to a mixture containing the electrochemically active gases CO and H_2. At the same time inside the anode the shift reaction takes place. The product gases diffuse deeper into the anode. At the TPB, which is replaced in the model by the last layer of grid nodes in the anode, H_2

* Electrochemical Society Active Member.
[a] Present address: Center for Solar Energy and Hydrogen Research Baden-Wuerttemberg, Ulm, Germany.
[z] E-mail: l.g.j.de.haart@fz-juelich.de

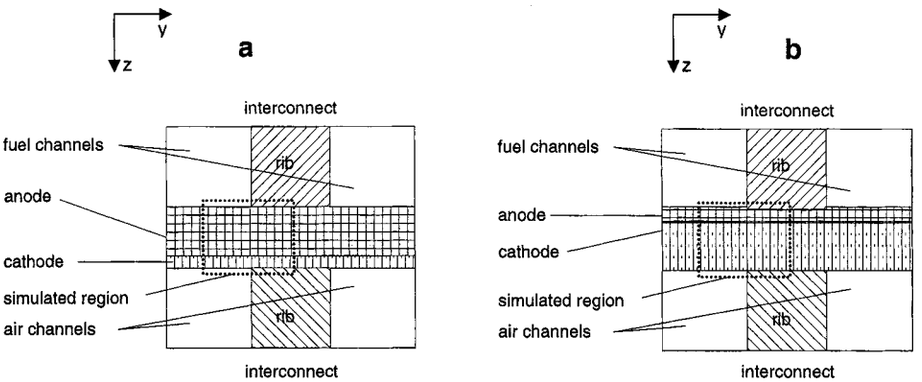

Figure 1. Schematic diagram of a planar SOFC based on (a) an anode substrate concept and (b) a cathode substrate concept. Dashed regions indicate the balance room considered in the simulation calculations.

and CO are oxidized. The electrolyte is simplified and integrated as a surface. In both cases the interconnect is not truncated.

The coordinate system is fixed for all simulations, where x is the direction of the gas flow in the channels, y is the direction in the cell plane perpendicular to the gas flow channel, and z the direction normal to the cell plane. The origin is fixed at the intersection point of the anode and the middle of the gas channel entrance. All simulations for two-dimensional cases are performed at the entrance of the gas/air channel, *i.e.*, at $x = 0$.

Mass transport.—The MTPM[12] is used to describe the mass transport of the gases in the porous substrate. This model is based on the assumption that the structure of the porous medium is isotropic. The porous structure can be described by three structural parameters: (*i*) Ψ: the ratio of porosity (ε) to tortuosity (τ); (*ii*) $\langle r\rangle$: the mean value of pore radii; and (*iii*) $\langle r^2\rangle$: the mean value of squared pore radii.

The conservation of mass for all components i in the porous medium, where both mass transport (molar flux density N_i) and chemical reactions (reaction rate R_i) occur, is given by

$$\frac{\psi}{RT}\frac{d(y_i p_g)}{dt} = -\nabla\cdot N_i + R_i \qquad [1]$$

Table I. Physical parameters.

Fuel cell geometry	Anode substrate	Cathode substrate
Anode thickness, dA [m]	1.5×10^{-3}	60×10^{-6}
Cathode thickness, dK [m]	40×10^{-6}	0.6×10^{-3}
Electrolyte thickness, dEl [m]	$0(17 \times 10^{-6})$	$0(17 \times 10^{-6})$
Fuel channel width, [m]	1.5×10^{-3}	1.5×10^{-3}
Oxidant channel width, [m]	1.5×10^{-3}	1.5×10^{-3}
Rib width fuel side, [m]	1.5×10^{-3}	1.5×10^{-3}
Rib width oxidant side, [m]	1.5×10^{-3}	1.5×10^{-3}

Fuel cell operation

Fuel gas composition, y_i [mol/mol]	CH_4	CO	H_2O	H_2	CO_2
	0.171	0.023	0.473	0.283	0.050
Oxidant gas composition, y_i [mol/mol]	O_2	N_2			
	0.21	0.79			
Fuel gas inlet temperature, [K]	973				
Oxidant gas inlet temperature, [K]	973				
Interconnect wall temperature, [K]	973				
Heat conductivity coefficient, λ [W/mK]	3				
Cell voltage, U [V]	0.7				

where y_i is the mole fraction of component i, p_g is the total pressure, R is the gas constant, and T the absolute temperature. The porous nature of the medium is represented by the factor Ψ in the first term.

Within the MTPM the mass transport is described as the sum of a diffusion flux and a permeation flux

$$N_i = N_i^d + N_i^p \qquad [2]$$

Diffusion effects can be either molecular diffusion or Knudsen diffusion, depending on the size of the pores of the porous medium. In the transition region both types exist

$$\frac{N_i^d}{D_i^k} + \sum_{j=1}^{0}\frac{y_j\cdot N_i^d - y_i\cdot N_j^d}{D_{ij}^m} = -c_g\frac{dy_i}{dz} \qquad [3]$$

The first term of Eq. 3 describes the Knudsen diffusion. The second term describes the molecular diffusion and is derived from the Stefan-Maxwell equations.

The effective Knudsen and binary diffusion coefficients are calculated according to

$$D_i^k = \psi\langle r\rangle\frac{2}{3}\sqrt{\frac{8RT}{\pi M_i}} \qquad [4]$$

and

$$D_{ij}^m = \psi\cdot\frac{1.013\cdot 10^{-2}\cdot T^{1,75}\sqrt{\frac{1}{M_i}+\frac{1}{M_j}}}{p[(\Sigma U_i)^{1/3}+(\Sigma U_j)^{1/3}]^2} \qquad [5]$$

respectively. Explanation of the symbols in the Eq. 4 and 5 and following can be found in the List of Symbols.

The permeation flux density is described by Darcy's Law

$$N_i^p = -\frac{B_i}{RT}\frac{dp}{dz} \qquad [6]$$

where the permeability coefficient B_i is determined by the Weber-equation[12]

$$B_i = D_i^k\left(\frac{K_{n_i}}{1+K_{n_i}}\right) + D_i^k\frac{\varpi m_{rel,i}}{1+K_i} + \frac{\langle r^2\rangle\Psi p_g}{8\eta_g} \qquad [7]$$

where $m_{rel,i}$ is the relative molar mass

$$m_{rel,i} = \sqrt{\frac{M_i}{\Sigma y_j M_j}} \qquad [8]$$

The MTPM summarizes all mass-transport phenomena in a concentration-dependent matrix **G**. The overall mass transport can be calculated by

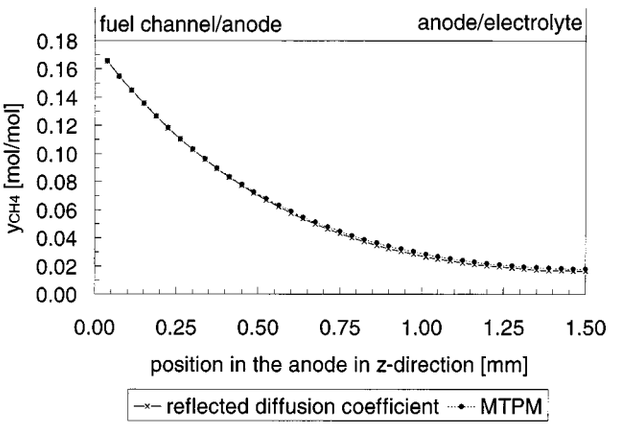

Figure 2. Methane concentration profile in a thick anode substrate for a one-dimensional simulation, comparing exact calculations and approximated reflected diffusion coefficient (see text for explanation).

$$\mathbf{N} = -[\mathbf{G}(c)]\frac{d\mathbf{c}}{dz} \quad [9]$$

$$N_i = g_{i1}\frac{dc_1}{dz} + g_{i2}\frac{dc_2}{dz} + \ldots + g_{in}\frac{dc_n}{dz} \quad [10]$$

In Eq. 10 the mass transport flux N_i of one species depends on the concentration gradients of all components. The one-dimensional simulation model[13,14] uses the exact MTPM Eq. 9 and 10. In the two-dimensional model the fluxes of each species were calculated using an approximation for the diffusion coefficient $D_{ref,i}$

$$\frac{N_i}{\left(\frac{dc_i}{dz}\right)} = D_{ref,i} \quad [11]$$

These so-called reflected diffusion coefficients were calculated from Eq. 9 and 10 for special boundary conditions, which enclose fraction of species and structural parameters. The use of the reflected diffusion coefficients was validated in a one-dimensional simulation case in comparison with the same simulation calculated with the exact Eq. 9 and 10. Figure 2 shows the concentration profile for methane in a porous anode substrate at the entrance of the fuel channel. A good agreement can be observed between the simulation with the approximated values for the diffusion constant and the exact calculated values. A similar agreement was observed for the other gases.

Reaction kinetics.—During operation of the fuel cell with natural gas, both the endothermic methane/steam reforming Reaction 12 and the exothermic shift Reaction 13, take place in the anode and in the gas phase, respectively

$$CH_4 + H_2O \rightleftharpoons CO + 3H_2 \quad [12]$$

$$CO + H_2O \rightleftharpoons CO_2 + H_2 \quad [13]$$

For the description of the reforming reaction a Hougan-Watson term is inserted[15]

$$R_1 = \frac{kK_{CH_4}K_{H_2O}p_{CH_4}p_{H_2O}}{(1 + K_{CH_4}p_{CH_4} + K_{H_2O}p_{H_2O})^2} \quad [14]$$

Recent experiments have verified the estimation of an equilibrium for all components effected by the shift reaction.[16]

The electrochemical conversion of H_2 and CO is integrated in the model according to Faraday's law

$$R_{el,H_2} = \frac{i_{H_2}}{z_e F} \quad [15]$$

$$R_{el,CO} = \frac{i_{CO}}{z_e F} \quad [16]$$

where the total current passing through the cell is $i_{H_2} + i_{CO}$. The current densities can be calculated from voltage and amperage with an equivalent circuit.[16] The electrochemical reactions have an exothermic character and are producing heat.

Heat transport.—The basic energy equation[17] for porous media describes different phenomena such as heat convection by the fluid and heat conduction in the solid

$$c_p\left(\frac{\delta T}{\delta t} + u\frac{\delta T}{\delta x} + v\frac{\delta T}{\delta y} + w\frac{\delta T}{\delta z}\right) = \lambda_{eff}\left(\frac{\delta^2 T}{\delta x^2} + \frac{\delta^2 T}{\delta y^2} + \frac{\delta^2 T}{\delta z^2}\right) + q + \phi \quad [17]$$

where q is an energy source term reflecting both the exothermic and endothermic reactions and ϕ is a term accounting for energy dissipation.

Because only steady-state simulations are performed, the time-dependent first term can be set to zero. The effective thermal conductivity coefficient λ_{eff} consists of a solid and a fluid conduction part

$$\lambda_{eff} = \varepsilon\lambda_f + (1 - \varepsilon)\lambda_s \quad [18]$$

In a first estimation the Peclet number was calculated inside the anode and results showed that heat transport by convection is negligible in comparison with the predominating thermal conduction, where experimentally determined values for the effective thermal conductivity coefficient of the anode material[18] were used.

Parameter values and boundary conditions.—The parameter values used in the following simulations are summarized in Table I. A cell voltage of 0.7 V is used as boundary condition. The fuel gas composition used represents a partially (30%) prereformed methane/steam (33/67 vol %/vol %) mixture.

The structural parameters for porous substrates used in the MTPM were determined by diffusion and permeation experiments.[19,20] Anode substrates (Ni/yttrium stabilized zironia (YSZ) cermets) manufactured at the Forschungszentrum Jülich were characterized previously.[13,21] Structural parameters for a standard anode substrate NZ40 are listed in Table II. Cathode substrates (Sr-doped $LaMnO_3$) were kindly supplied by the University of Karlsruhe. The cathode samples were around 400 μm thick and were sintered between 1200 and 1300°C. Higher sintering temperatures lead to an increased density of the samples. Figure 3 shows that with this increasing density the average pore size decreases. Figure 4 shows the values of the factor Ψ (porosity/tortuosity) in dependence of the density and sintering temperature. T1200 is sintered at 1200°C and shows the highest factor Ψ as well as the highest pore radius of this production series. T1275, sintered at 1275°C, is a probe with an average Ψ and pore radius. Because of the substantial differences depending on the production series, structural parameters from two different cathode substrate series, as listed in Table II, were selected for the simulations.

Because these structural parameters could be determined only for thick substrates, the same values were used for the thin anode and cathode layers in the cathode substrate and anode substrate, respectively.

For each of these substrates the one-dimensional mass transport according to the exact MTPM Eq. 9 and 10 was simulated using the software tool MATLAB. The reflected diffusion coefficients were calculated for the boundary conditions chosen with Eq. 11. The values for the reflected diffusion coefficients, listed in Table II, are used in the two-dimensional simulation in FLUENT.

Table II. Structural parameter and reflected diffusion coefficient.

				D_i for T = 973-1123 K				
Anode substrate sample	Ψ	$\langle r \rangle$ (m)	$\langle r^2 \rangle$ (m^2)	D_{CH4} ($m^2\ s^{-1}$)	D_{CO} ($m^2\ s^{-1}$)	D_{H2O} ($m^2\ s^{-1}$)	D_{H2} ($m^2\ s^{-1}$)	D_{CO2} ($m^2\ s^{-1}$)
NZ40	0.156	1.07×10^{-6}	3.8×10^{-13}	2.8×10^{-5}	2.6×10^{-5}	3×10^{-5}	9.5×10^{-5}	2.3×10^{-5}
Cathode substrate sample	Ψ	$\langle r \rangle$ (m)	$\langle r^2 \rangle$ (m^2)	D_{O2} $/m^2s^{-1}$				
A65a	0.037	2.34×10^{-6}	8.6×10^{-13}	6.6×10^{-6}				
T1200	0.028	3.05×10^{-6}	1.21×10^{-12}	5.2×10^{-6}				
T1275	0.021	1.09×10^{-6}	5.61×10^{-13}	3.2×10^{-6}				

For the cathode substrates the variation in the structural parameters shows that the reflected diffusion coefficient decreases with higher sintering temperatures. The main influence on the reflected diffusion coefficient was the structural parameter Ψ. Sample A65a refers to another production series sintered at 1200°C with a thickness of about 600 μm. The property of T1200 is a higher average pore size radius and a higher average square compared to A65a, but the lower factor Ψ results in a lower reflected diffusion coefficient.

Results and Discussion

Two-dimensional cases were simulated for both types of anode and cathode substrate concept SOFC operating on prereformed methane. Figure 5 shows the resulting concentration profiles for methane, hydrogen, and air as well as the temperature distribution in both cases. Particularly in Fig. 5a the fast reforming reaction is reflected by the methane distribution in the porous medium of the anode substrate. A large amount of methane already reacts in the boundary region near the gas channel. Detailed one-dimensional analysis shows the reforming reaction to be confined in a region extending only up to around 300 μm into the anode (z direction) at the center of the gas channel. This depth is even less below the center of the rib. There is hardly any methane reaching the anode/electrolyte interface. However, the anode/electrolyte interface is sufficiently supplied with hydrogen resulting from the methane/steam reforming reaction, as can be seen in Fig. 5b.

Depending on the degree of prereforming, different temperature gradients arise in the anode substrate. The temperature distribution inside the anode (Fig. 5d) reveals a maximum temperature of around 973 K and a minimum temperature of around 971.5 K, which is situated around 0.5 mm in the z direction from the gas channel at the center of the channel. With the assumption of a linear distribution, a temperature gradient of around 2-3 K/mm can be calculated. Recent one-dimensional simulations[14] have shown similar gradients but for higher boundary temperatures using a slower reforming kinetic. The distribution and steepness of the temperature curve depend not only on the boundary conditions and reaction kinetics, but also on the properties of the electrodes, that is, the effective heat conductivity, as was shown in a previous study.[14] At the interface region anode/fuel channel the gradient can be higher due to truncation.

The boundary conditions are valid for coflow operation with a homogeneous temperature (T = 973.15 K) at the interfaces of both electrodes with the channels and with the interconnect. Because channel and interconnect are cut in the middle, adiabatic conditions exist at the edges of this balance room.

In the cathode substrate concept the temperature profile in the solid is more homogeneous (Fig. 5h), so that only very small temperature gradients arise. More problematic is the oxygen distribution in the cathode substrate. The oxygen molar fraction decreases from 0.21 at the air channel side to 0.07 under the interconnect (Fig. 5g). For this case the better structural parameters of sample A65a have been used in the calculation of the reflected diffusion coefficient. For a lower porosity and a higher sintering temperature the depletion of oxygen results in an oxygen molar fraction close to zero at the cathode/electrolyte interface.

In Fig. 6 the local current density profile at the cathode/electrolyte interface is shown for the simulation case with type A65a cathode substrate. The current density profile shows a maximum above the center of the air channel (y = 0) and drops to a minimum below the center of the interconnect rib. The diffusion of oxygen in the thin cathode layer for which the same structural parameters are assumed in the anode substrate case is even more hampered below the interconnect ribs, as can be seen from the corresponding local current density profile shown in Fig. 7. Part of the anode/electrolyte interface is electrochemically inactive due to the depletion of oxygen below the interconnect rib. Here the question must be put forward, whether it is allowed to use the structural parameters determined for relatively thick substrates for these thin (50 μm) electrode

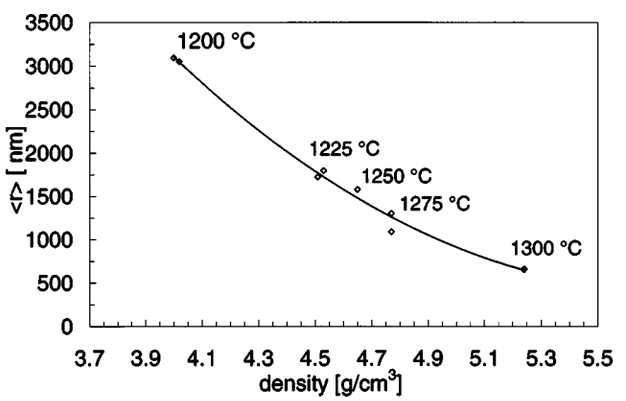

Figure 3. Mean value of pore radii as function of density and sintering temperature determined for several cathode substrates.

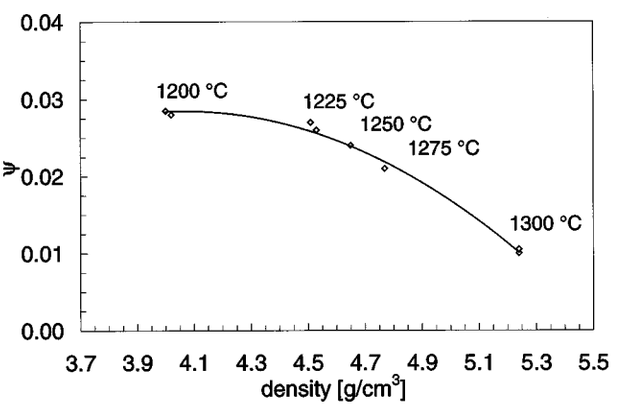

Figure 4. Value of the factor Ψ [ratio of porosity (ε) to tortuosity (τ)] as function of density and sintering temperature determined for several cathode substrates.

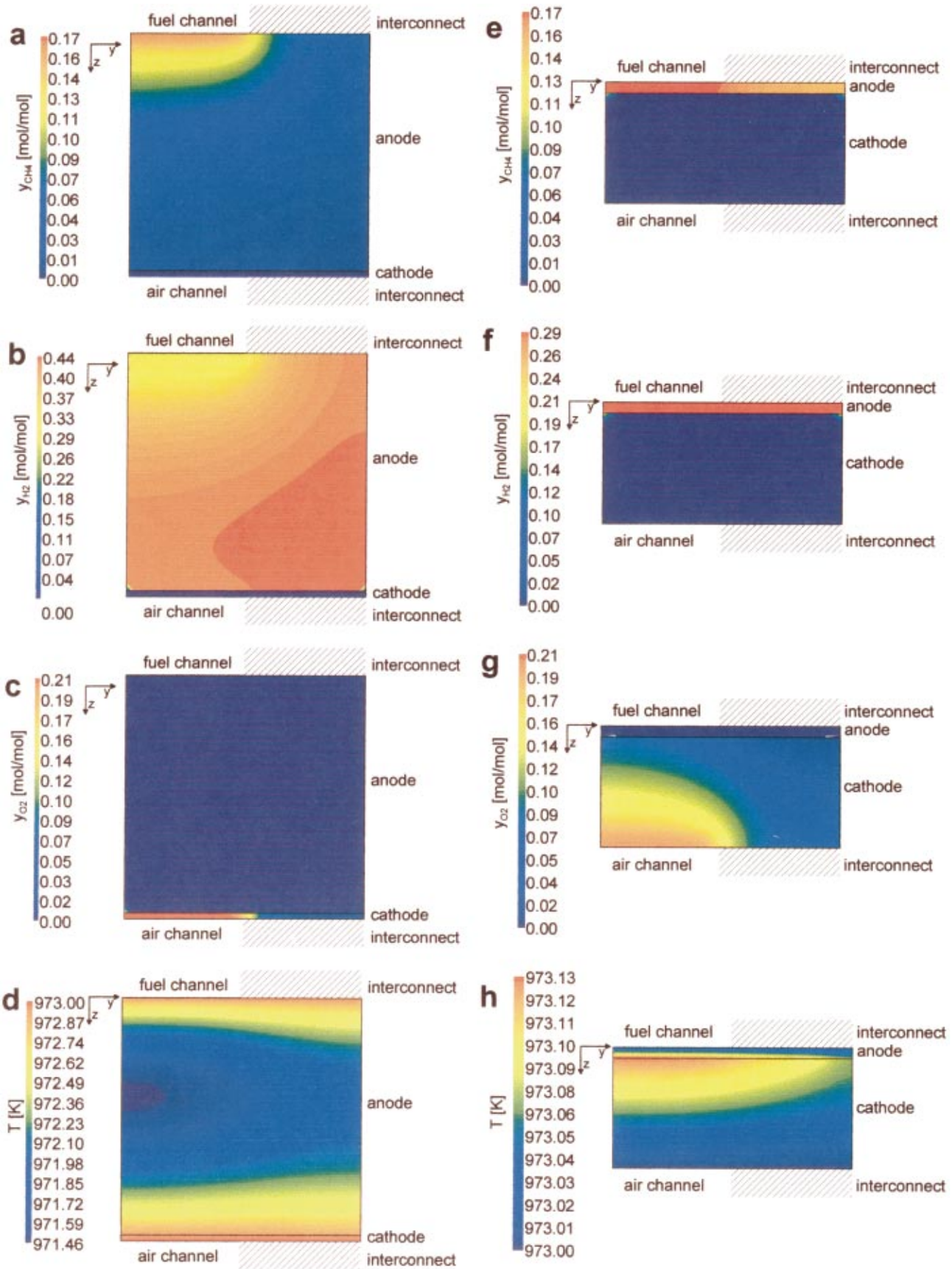

Figure 5. Simulated two-dimensional concentration profiles of (a, e) methane, (b, f) hydrogen, and (c, g) oxygen and (d, h) temperature profiles in (a-d) an anode substrate concept and (e-h) a cathode substrate concept SOFC.

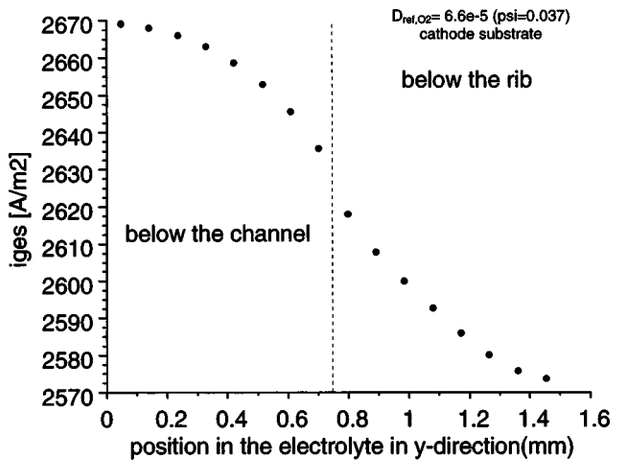

Figure 6. Local current density profile at the cathode/electrolyte interface for the cathode substrate case.

layers as well. Also one could place a question mark at the structural parameters for the cathode substrates determined in this study. There is some difference between the parameters obtained for the cathode substrates and the anode substrate. In particular the values for Ψ [ratio of porosity (ε) to tortuosity (τ)] ranging from 0.021 to 0.037 seem low. With a tortuosity of 3, which is not uncommon for ceramics, the open porosity is only between 6 and 11%. Thin cathode layers, as known from our own anode substrate concept, have higher porosity values. Further experiments will be performed to validate the structural parameters for these kind of cathode substrates.

Conclusions

A mathematical model has been developed, that offers the possibility of determining temperature and concentration profiles in porous substrates of an SOFC. The mass transport in the porous substrates is described by the MTPM. The necessary structural parameters could be obtained by diffusion and permeation experiments. First two-dimensional simulations of substrate type SOFC operating on partially prereformed methane reveal diffusion limitation of oxygen in the cathode. This may be attributed to the low porosity-to-tortuosity ratio determined for the cathode substrates.

The model will be used to perform a sensitivity analysis of selected parameters. This will enable an optimization of the mass transport inside the electrode by changing the structural parameters with respect to the performance of a fuel cell. The results of this optimization can have a direct influence on manufacturing methods and/or conditions. In a next step an extension to the third dimension is planned.

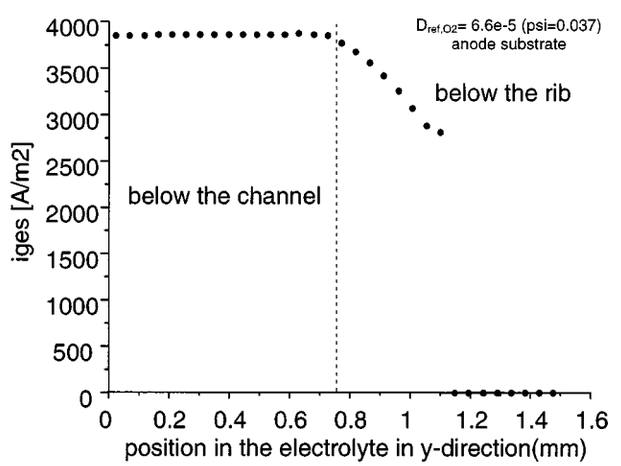

Figure 7. Local current density profile at the anode/electrolyte interface for the anode substrate case.

Acknowledgments

Financial support by the Deutsche Forschungsgemeinschaft under contract no. LE 1139/1-1 and HA 2842/1-2 is gratefully acknowledged. The authors also thank A. Weber of the University of Karlsruhe for the kind supply of cathode substrates and R. Rommerskirchen for performing the diffusion and permeation experiments.

Forschungszentrum Jülich GmbH assisted in meeting the publication costs of this article.

List of symbols

B	permeability coefficient, m^2/s
c	molar concentration, mol/m^3
c_p	molar heat capacity, J/mol/K
dA	thickness anode, m
dEl	thickness electrolyte, m
dK	thickness cathode, m
d/dx	differential coefficient
D	diffusion coefficient, m^2/s
D^k	effective Knudsen diffusion coefficient, m^2/s
D^m	effective molar diffusion coefficient, m^2/s
F	Faraday constant, A s/mol
k	reaction rate constant, $kmol_{CH4}/mol_{Ni}/s$
Kn_i	Knudsen number=average molecular path length/(2 × pore radius)
K_i	adsorption equilibrium constant, 1000/Pa
m_{rel}	relative molar weight
M	molar mass, kg/kmol
N	molar flux density, $mol/m^2/s$
N^d	molar diffusion flux density, $mol/m^2/s$
N^p	molar permeation flux density, $mol/m^2/s$
p	pressure, Pa
$\langle r \rangle$	mean value of pore radii, m
$\langle r^2 \rangle$	mean value of squared pore radii, m^2
R	gas constant, 8.314 J/mol/K
R_i	reaction rate, $mol/m^3/s$
q	source and drain term, W/m^3
t	time, s
T	temperature, K
u, v, w	velocity in x, y, z direction, m/s
dx	length, m
y	mole fraction, mol/mol
z_e	number of electrons

Greek

ε	porosity
ϕ	energy dissipation, W/m^3
η	viscosity, kg/m/s
λ	thermal conductivity, W/m/K
τ	tortuosity
υ	diffusion volume
ω	$\pi/4$
Ψ	ε/τ

Subscripts

el	electrochemical
f	fluid phase
i	species
j	species II
g	total
ref	reflected
s	solid phase

References

1. E. Achenbach and U. Reus, in *Solid Oxide Fuel Cells VI*, S. C. Singhal and M. Dokiya, Editors, PV 99-19, p. 1125, The Electrochemical Society Proceedings Series, Pennington, NJ (1999).
2. J. Yuan, M. Rokni, and B. Sundén, in *Solid Oxide Fuel Cells VI*, S. C. Singhal and M. Dokiya, Editors, PV 99-19, p. 1099, The Electrochemical Society Proceedings Series, Pennington, NJ (1999).
3. J. Hartvigsen, A. Khandkar, and S. Elangovan, in *Solid Oxide Fuel Cells VI*, S. C. Singhal and M. Dokiya, Editors, PV 99-19, p. 1135, The Electrochemical Society Proceedings Series, Pennington, NJ (1999).

4. H. Yakabe, T. Ogiwara, and I. Yasuda, in *Solid Oxide Fuel Cells VII*, H. Yokokawa and S. C. Singhal, Editors, PV 2001-16, p. 1022, The Electrochemical Society Proceedings Series, Pennington, NJ (2001).
5. M. A. Khaleel, K. P. Recknagle, Z. Lin, J. E. Deibler, L. A. Chick, and J. W. Stevenson, in *Solid Oxide Fuel Cells VII*, H. Yokokawa and S. C. Singhal, Editors, PV 2001-16, p. 1032, The Electrochemical Society Proceedings Series, Pennington, NJ (2001).
6. H. P. Buchkremer, U. Diekmann, L. G. J. de Haart, H. Kabs, U. Stimming, and D. Stöver, in *Solid Oxide Fuel Cells V*, U. Stimming, S. C. Singhal, H. Tagawa, and W. Lehnert, Editors, PV 97-40, p. 160, The Electrochemical Society Proceedings Series, Pennington, NJ (1997).
7. K. Föger, R. Donelson, and R. Ratnaraj, in *Solid Oxide Fuel Cells VI*, S. C. Singhal and M. Dokiya, Editors, PV 99-19, p. 95, The Electrochemical Society Proceedings Series, Pennington, NJ (1999).
8. D. Ghosh, G. Wang, R. Brule, E. Tang, and P. Huang, in *Solid Oxide Fuel Cells VI*, S. C. Singhal and M. Dokiya, Editors, PV 99-19, p. 822, The Electrochemical Society Proceedings Series, Pennington, NJ (1999).
9. J. P. Ouweltjes, F. P. F. van Berkel, P. Nammensma, and G. M. Christie, in *Solid Oxide Fuel Cells VI*, S. C. Singhal and M. Dokiya, Editors, PV 99-19, p. 803, The Electrochemical Society Proceedings Series, Pennington, NJ (1999).
10. H. Yakabe, M. Hishinuma, M. Uratani, Y. Matsuzaki, and I. Yasuda, *J. Power Sources*, **86**, 423 (2000).
11. H. Yakabe, T. Ogiwara, M. Hishinuma, and I. Yasuda, *J. Power Sources*, **102**, 144 (2001).
12. D. Arnost and P. Schneider, *Chem. Eng. J.*, **57**, 91 (1995).
13. W. Lehnert, J. Meusinger, and F. Thom, *J. Power Sources*, **87**, 57 (2000).
14. T. Ackmann, L. G. J. de Haart, W. Lehnert, and F. Thom, in *Proceedings of the 4th European SOFC Forum*, Vol. 1, p. 431, European Fuel Cell Forum, Oberrohrdorf, Switzerland (2000).
15. I. Drescher, Jül-3699, Berichte des Forschungszentrums Jülich, D82 (Diss. RWTH Aachen, 1999).
16. Ch. Rechenauer, E. Achenbach, Jül-2752, Berichte des Forschungszentrums Jülich, D82 (Diss. RWTH Aachen, 1993).
17. R. H. Perry and D. W. Green, *Perry's Chemical Engineers' Handbook*, 7th ed., p. 5, MacGraw-Hill, New York (1997).
18. W. Hu, H. Guan, X. Sun, S. Li, M. Fukumoto, and I. Okane, *J. Am. Ceram. Soc.*, **81**, 2209 (1998).
19. P. Fott and G. Petrini, *Appl. Catal.*, **2**, 367 (1982).
20. J. Valus and P. Schneider, *Appl. Catal.*, **1**, 355 (1981).
21. I. Drescher, W. Lehnert, and J. Meusinger, *Electrochim. Acta*, **43**, 3059 (1998).